Supplementary Information

Stitchable Supercapacitors with High Energy Density and High Rate Capability Using Metal Nanoparticle-Assembled Cotton Threads†

Dongyeeb Shin[a], Cheong Hoon Kwon[a], Yongmin Ko[a,b], Byeongyong Lee[b], Seung Woo Lee*[b] and Jinhan Cho*[a]

[a]Department of Chemical and Biological Engineering, Korea University, 145 Anam-ro, Seongbuk-gu, Seoul 02841, Republic of Korea. *E-mail: jinhan71@korea.ac.kr

[b]The George W. Woodruff School of Mechanical Engineering, Georgia Institute of Technology, Atlanta, Georgia 30332, USA. *E-mail: seung.lee@me.gatech.edu.

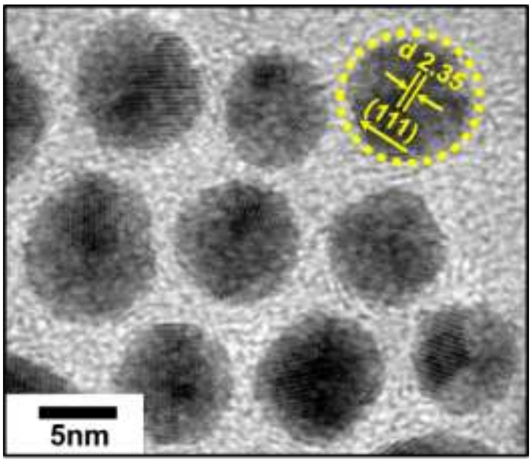

Fig. S1 HR-TEM image of the TOABr-Au NPs.

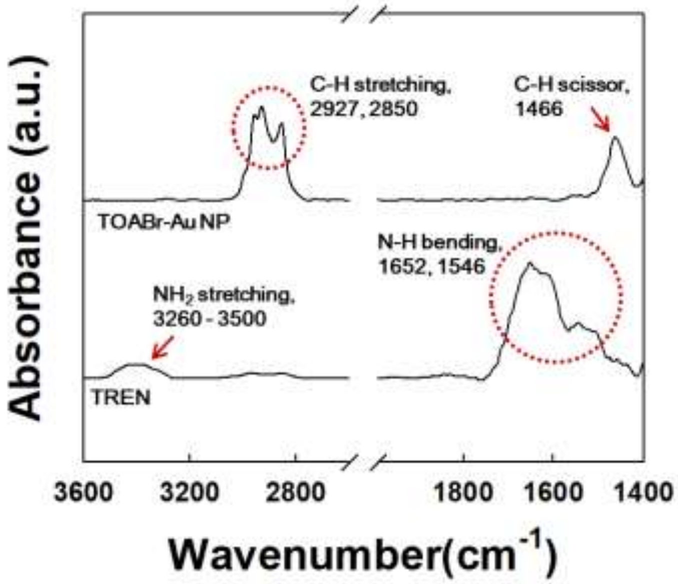

Fig. S2 Characteristic FTIR spectra of the TOABr-Au NPs and TREN.

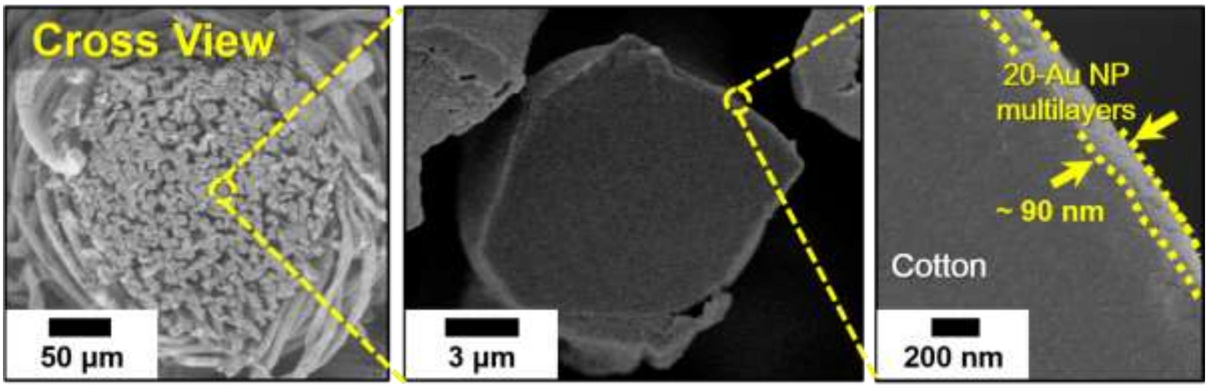

Fig. S3 Cross-sectional FE-SEM images of the (TREN/TOABr-Au NP)$_{20}$-coated cotton threads.

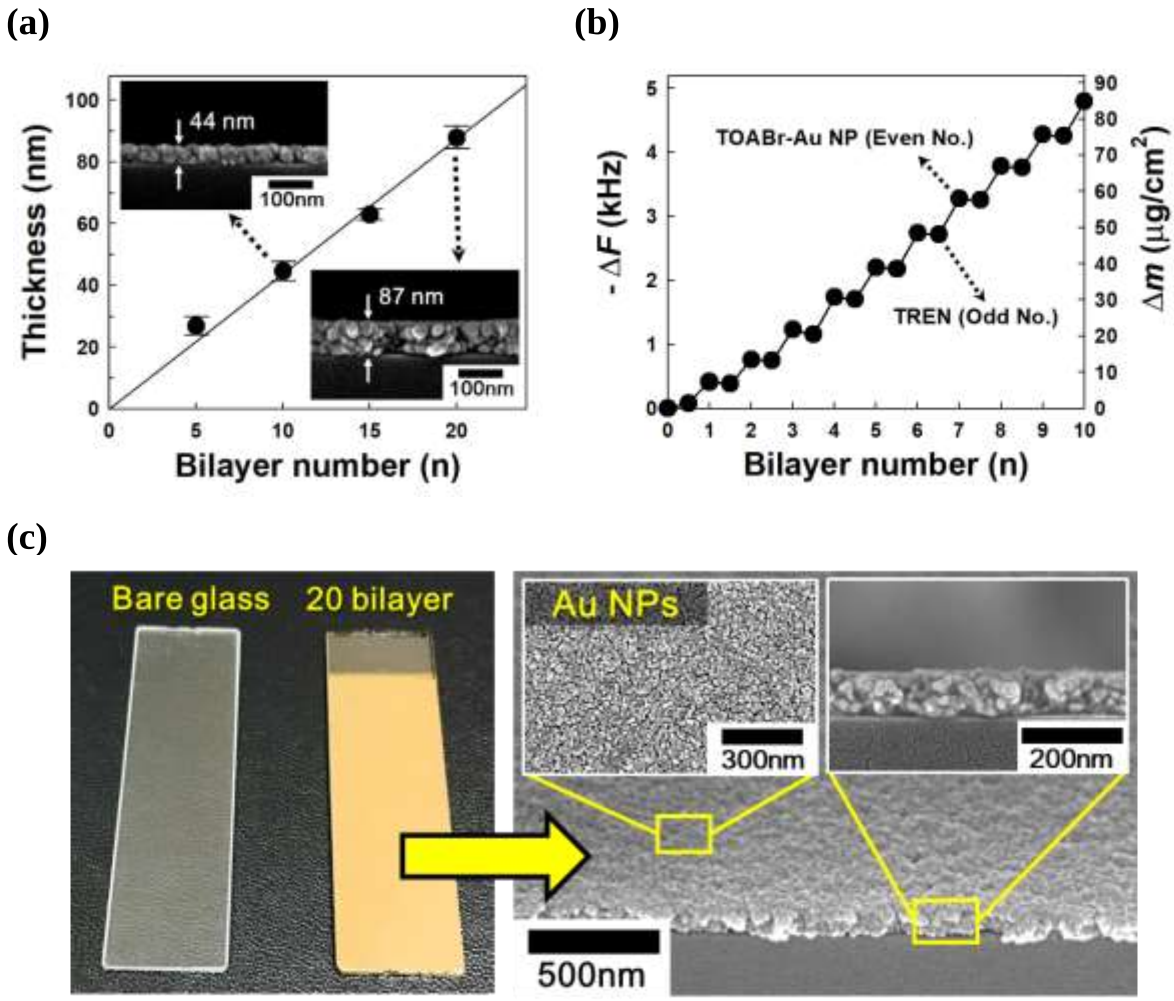

Fig. S4 (a) Film thickness, (b) frequency and mass change of the (TREN/TOABr-Au NP)$_n$ multilayers deposited onto nonporous flat substrates as a function of the bilayer number (n). (c) Photographs and FE-SEM images of the (TREN/TOABr-Au NP)$_{20}$ multilayers deposited onto nonporous flat substrates.

(a)

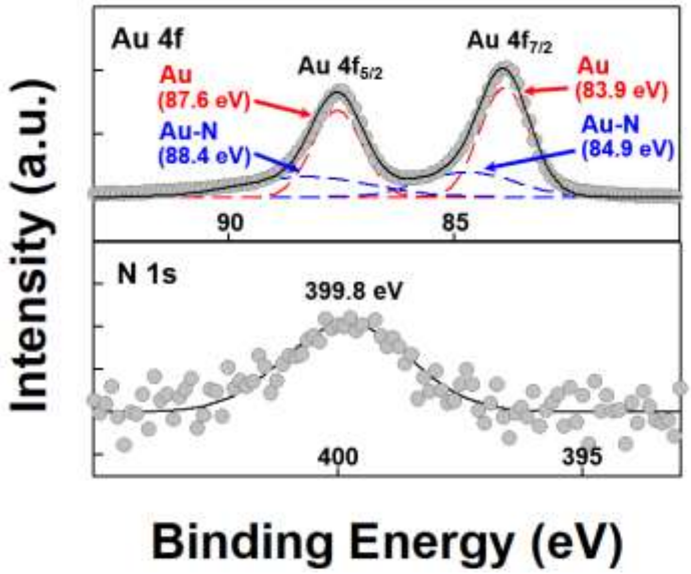

(b)

Elements	Au	N	C	O	Br
Atomic ratio (%)	45.2	7.5	34.6	10.4	2.3

Fig. S5 (a) XPS spectra analysis of (TREN/TOABr-Au NP)$_{20}$ multilayers. In this case, the Au 4f XPS spectrum shows the narrow two spin-orbital splitting of Au 4f$_{5/2}$ and Au 4f$_{7/2}$, and these characteristic peaks can also be deconvoluted into two pairs of spectra derived from bulk Au (at 87.6 and 83.9 eV) and Au-N bond (at 84.9 and 88.4 eV), respectively.[S1,S2] Additionally, N 1s spectrum at 399.8 eV is also consistent with previous reports that metal-amine bonds exhibit binding energies in the range of 398 to 400 eV.[S3,S4] (b) Atomic ratios of (TREN/TOABr-Au NP)$_{20}$ multilayer.

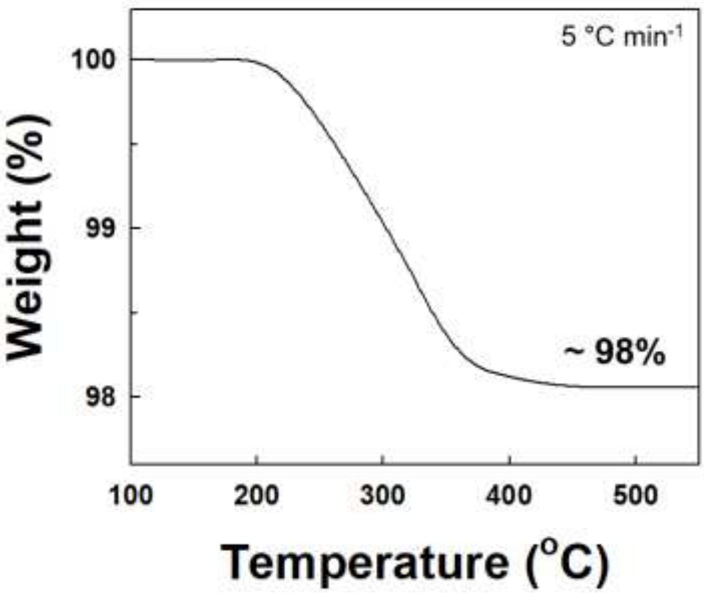

Fig. S6 Thermogravimetric analysis (TGA) of the (TREN/TOABr-Au NP)$_{20}$ multilayer with a heating rate of 5°C min^{-1} under nitrogen environment.

(a)

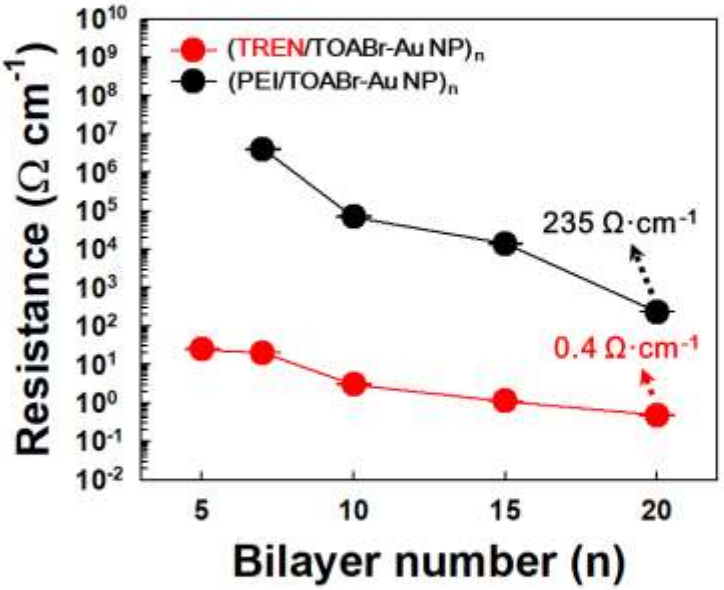

(b)

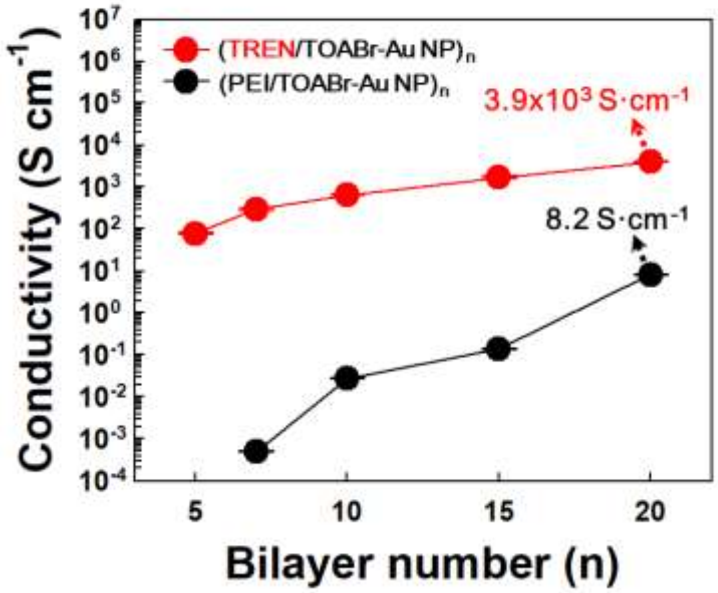

Fig. S7 (a) Resistance and (b) electrical conductivity of the (TREN/TOABr-Au NP)$_n$ and (PEI/TOABr-Au NP)$_n$ multilayer-coated cotton threads as a function of the bilayer number (n).

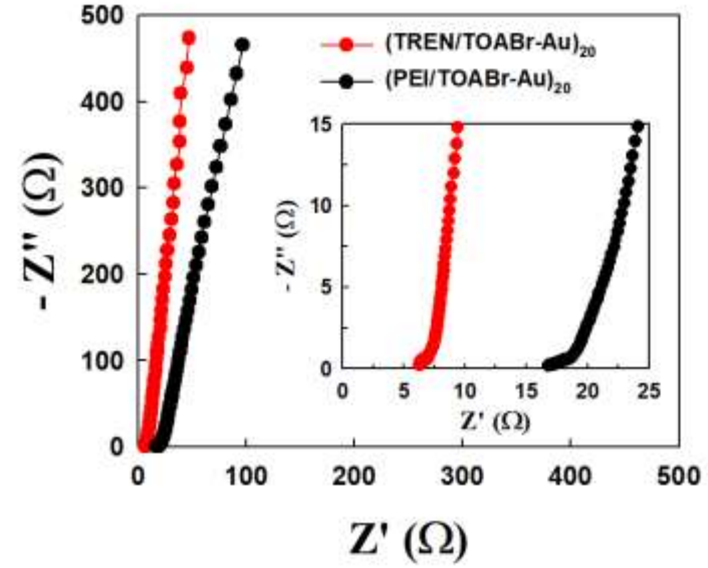

Fig. S8 Nyquist plots of the (TREN/TOABr-Au NP)$_{20}$ and (PEI/TOABr-Au NP)$_{20}$ multilayer-coated cotton threads.

(a) (b)

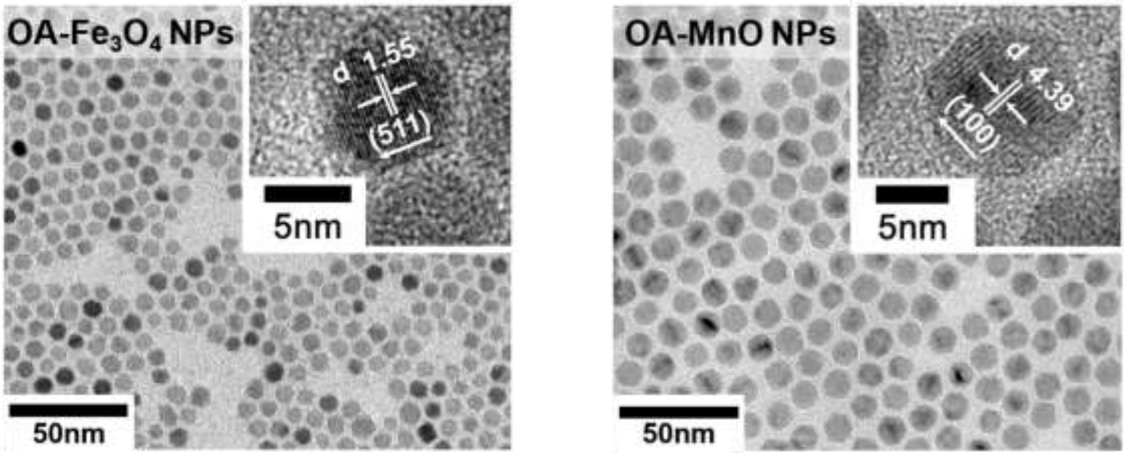

Fig. S9 (a) HR-TEM images of the OA-Fe_3O_4 NPs and (b) OA-MnO NPs.

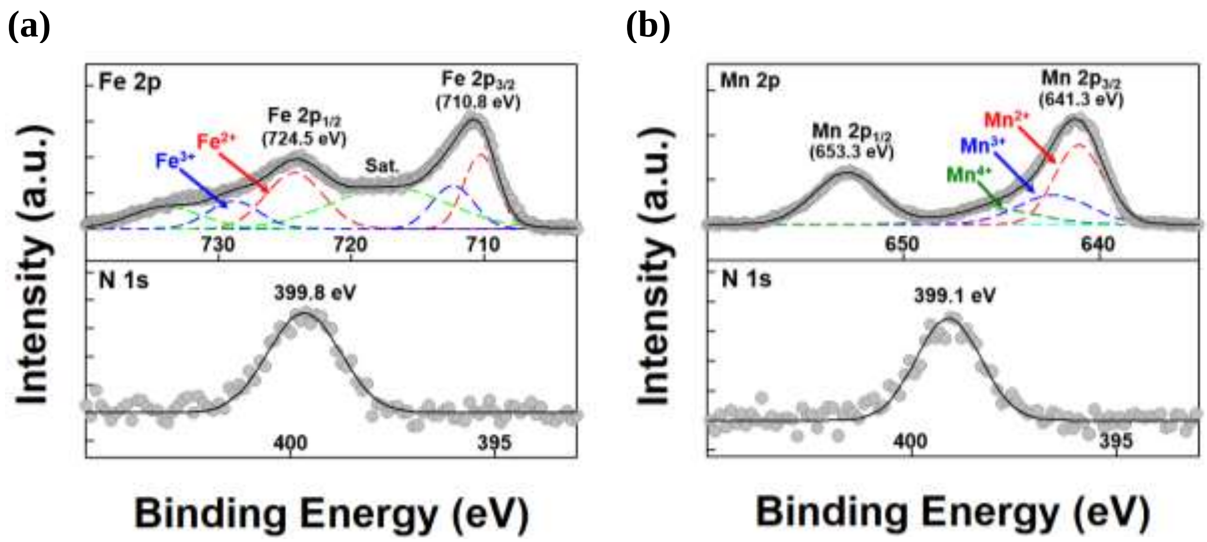

Fig. S10 (a) XPS analysis of the (TREN/OA-Fe_3O_4 NPs)$_{20}$ and (b) (TREN/OA-MnO NPs)$_{20}$ multilayers. The Fe2p spectrum of (TREN/OA-Fe_3O_4 NP)$_{20}$ multilayer exhibits two characteristic peaks at 710.8 eV for Fe2p$_{3/2}$ and 724.5 eV for Fe2p$_{1/2}$.[S5,S6] These Fe2p spectra can further be deconvoluted into two spectra of Fe^{2+} (710.7 and 724.3 eV) and Fe^{3+} (712.3 and 728.8 eV) of Fe species. In this case, the absence of a satellite peak at 717.2 eV was ascribed to a typical characteristic of Fe_3O_4.[S6,S7] The Mn2p spectrum of (TREN/OA-MnO NP)$_{20}$ multilayer showed two spin-orbitals of Mn 2p$_{3/2}$ (641.3 eV) and Mn 2p$_{1/2}$ (653.3 eV) involving multivalent Mn species (Mn^{2+}, Mn^{3+}, and Mn^{4+}), indicating the typical oxidation state of MnO.[S8,S9,S10] Furthermore, the N 1s peaks of the OA-Fe_3O_4- and MnO NP-based multilayers in the ranges of 398 − 400 eV also demonstrate the metal-N bonds.[S3,S4]

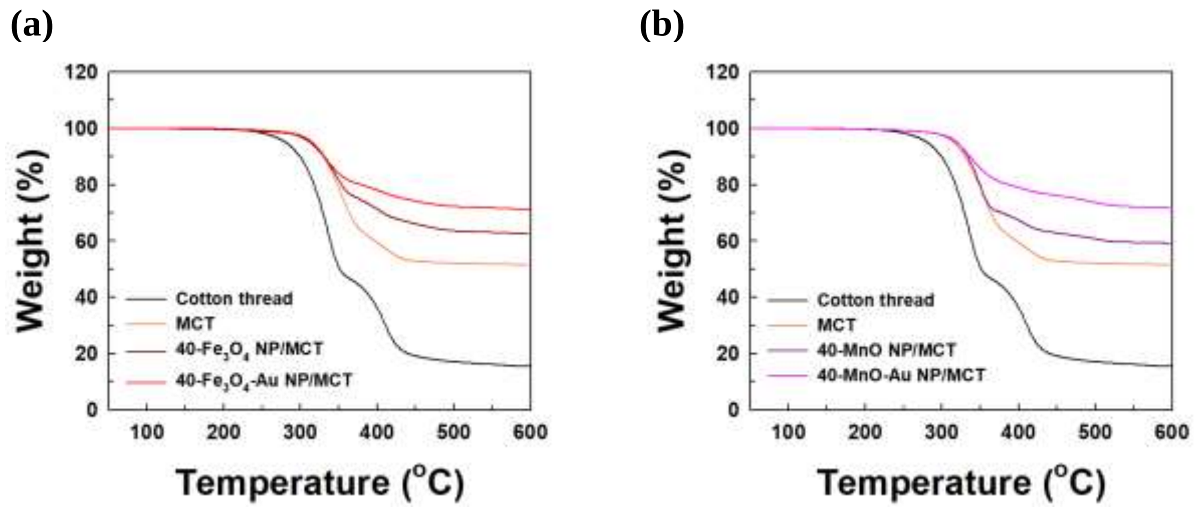

Fig. S11 (a) TGA of the Fe_3O_4 NPs-based and (b) MnO NPs-based thread electrodes with a heating rate of 5°C min^{-1} under nitrogen environment. The residual amounts of the cotton thread, MCT, 40-Fe_3O_4 NP/MCT and 40-Fe_3O_4-Au NP/MCT were measured to be approximately 0.095 mg·cm^{-1} (15.4 %, **ash**), 0.57 mg·cm^{-1} (52.3 %, **ash + 20-Au NP**), 0.88 mg·cm^{-1} (62.2 %, **ash + 20-Au NP + 40-Fe_3O_4 NP**), and 1.31 mg·cm^{-1} (70.8 %, **ash + 20-Au NP + 40-Fe_3O_4 NP + Inserted Au NP**), respectively. In case of 40-MnO NP/MCT and 40-MnO-Au NP/MCT, their residual amounts were estimated to be 0.85 mg·cm^{-1} (61.4 %, **ash + 20-Au NP + 40-MnO NP**) and 1.27 mg·cm^{-1} (70.1 %, **ash + 20-Au NP + 40-MnO NP + Inserted Au NP**), respectively. As a result, the loading amount per length of 40-Fe_3O_4 and 40-MnO NPs in MCTs are 0.31 and 0.28 mg·cm^{-1}, respectively.

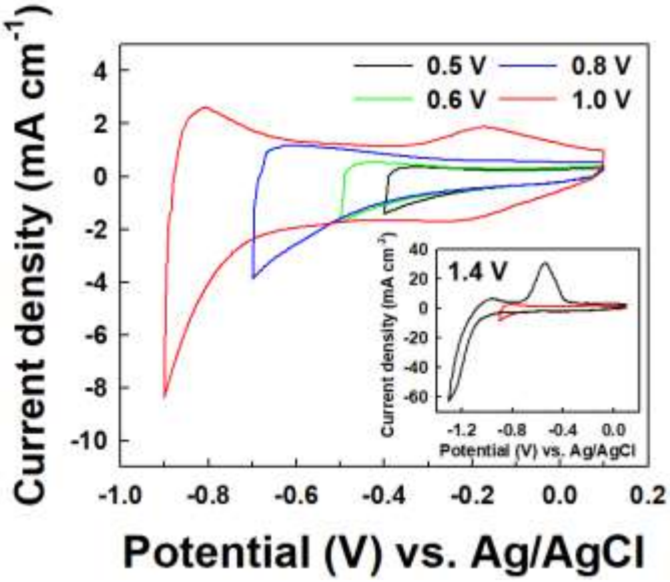

Fig. S12 CV scans of the 40-Fe_3O_4-Au NP/MCT over different potential regions from 0.5 to 1.4 V at a scan rate 5 mV s^{-1}.

(a)

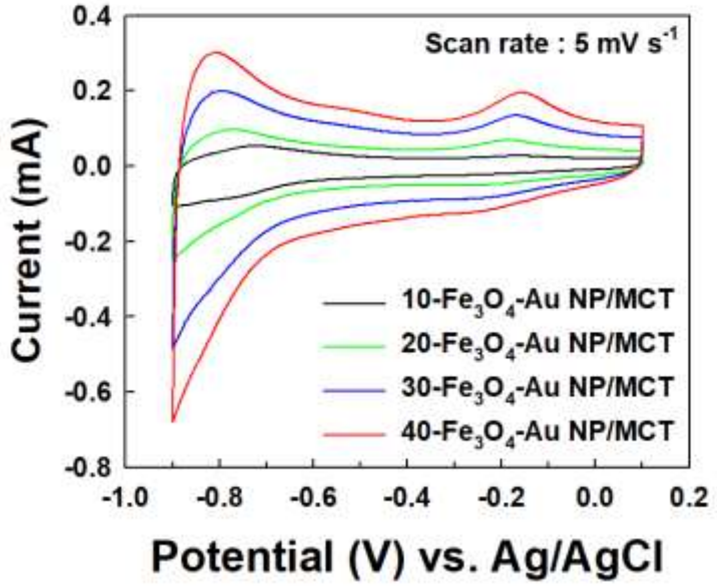

(b)

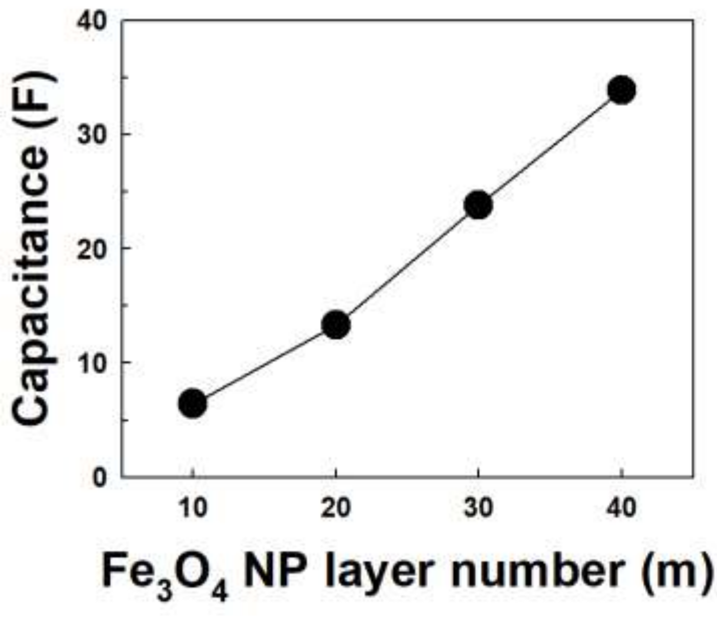

Fig. S13 (a) CV scans and (b) capacitance of the m-Fe_3O_4-Au NP/MCT electrodes as a function of the total Fe_3O_4 NP layer number (m) at a scan rate of 5 mV s^{-1}.

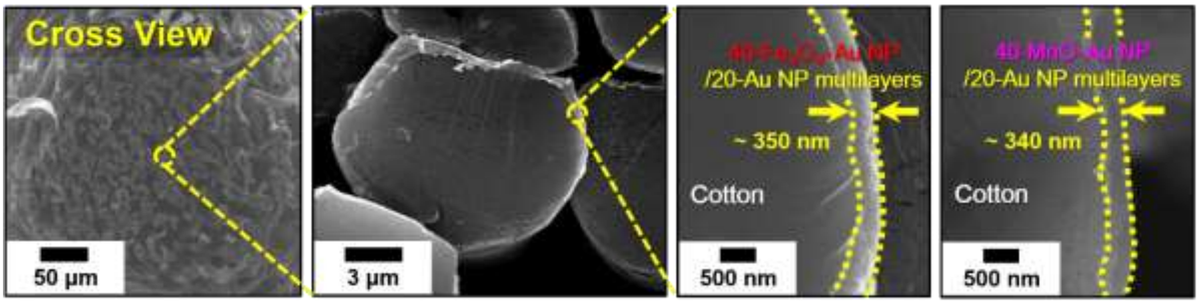

Fig. S14 Cross-sectional FE-SEM images of the 40-Fe_3O_4-Au NP/MCT and 40-MnO-Au NP/MCT electrodes.

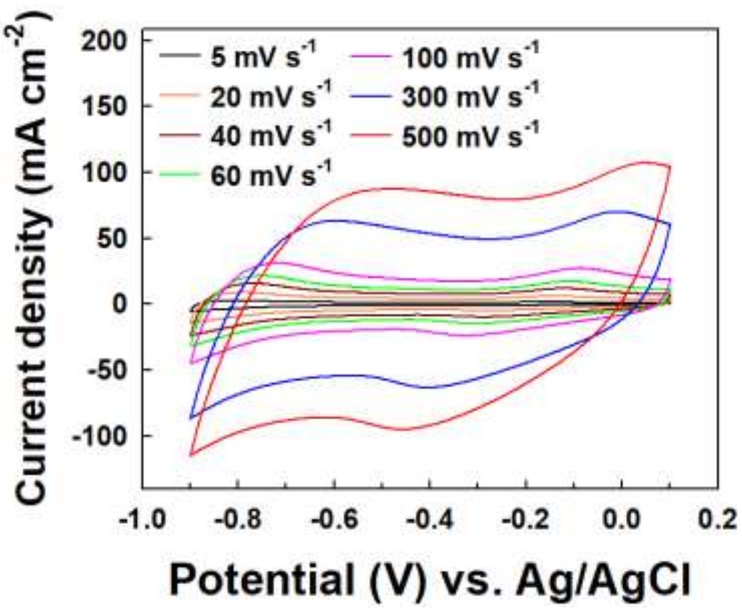

Fig. S15 CV scans of the 40-Fe_3O_4-Au NP/MCT electrodes at varied scan rate from 5 to 500 mV s^{-1}.

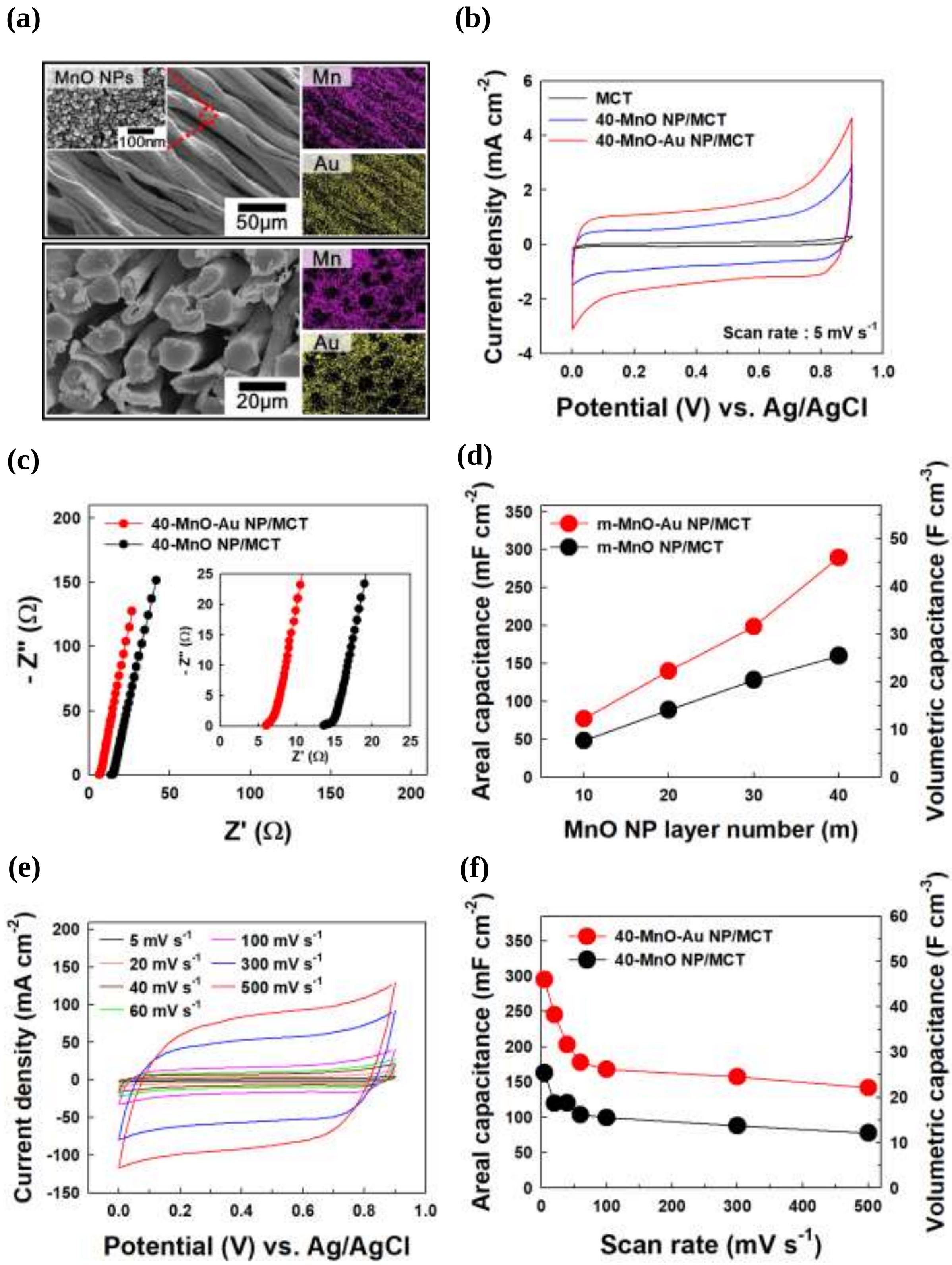
(a)
MnO NPs
100nm
50μm
Mn
Au
20μm
Mn
Au
(b)
MCT
40-MnO NP/MCT
40-MnO-Au NP/MCT
Scan rate : 5 mV s-1
Current density (mA cm-2)
Potential (V) vs. Ag/AgCl
(c)
40-MnO-Au NP/MCT
40-MnO NP/MCT
- Z'' (Ω)
Z' (Ω)
(d)
m-MnO-Au NP/MCT
m-MnO NP/MCT
Areal capacitance (mF cm-2)
Volumetric capacitance (F cm-3)
MnO NP layer number (m)
(e)
5 mV s-1
20 mV s-1
40 mV s-1
60 mV s-1
100 mV s-1
300 mV s-1
500 mV s-1
Current density (mA cm-2)
Potential (V) vs. Ag/AgCl
(f)
40-MnO-Au NP/MCT
40-MnO NP/MCT
Areal capacitance (mF cm-2)
Volumetric capacitance (F cm-3)
Scan rate (mV s-1)

Fig. S16 (a) FE-SEM and EDS mapping images of the 40-MnO-Au NP/MCT electrodes. (b) CV scans of the MCT, 40-MnO NP/MCT, and 40-MnO-Au NP/MCT electrodes at a scan rate of 5 mV s^{-1}. (c) Nyquist plots of the 40-MnO NP/MCT and 40-MnO-Au NP/MCT electrodes. (d) Areal and volumetric capacitances of the 40-MnO NP/MCT and 40-MnO-Au NP/MCT electrodes as a function of the total MnO NP layer number (m) at a scan rate of 5 mV s^{-1}. (e) CV scans of the 40-MnO-Au NP/MCT electrodes with increasing scan rate from 5 to 500 mV s^{-1}. (f) Areal and volumetric capacitances of the 40-MnO NP/MCT and 40-MnO-Au NP/MCT electrodes as a function of the scan rate.

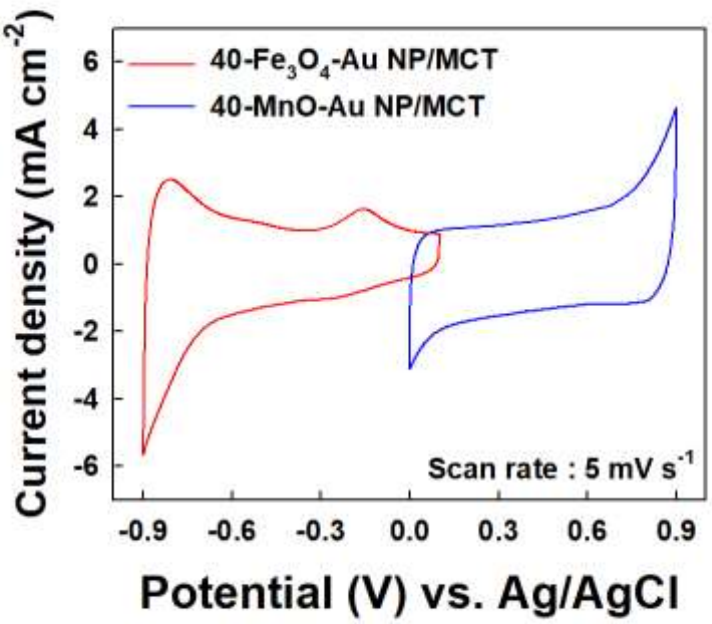

Fig. S17 CV scans of the 40-Fe_3O_4-Au NP/MCT and 40-MnO-Au NP/MCT electrodes at a scan rate of 5 mV s^{-1}. The charge balance ($q^+ = q^-$) between the 40-Fe_3O_4-Au NP/MCT (negative electrode) and 40-MnO-Au NP/MCT (positive electrode) follows the relationship: S11

$$A^+/A^- = C^-\Delta V^-/C^+\Delta V^+ \ (q = C \times \Delta V \times A)$$

where q is the stored charge, C is the specific capacitance, ΔV is the voltage window, and A is the surface area of the electrode. On the basis of this equation, the length ratio between the two electrodes (i.e., L(Fe_3O_4)/L(MnO)) was calculated to be approximately 0.95.

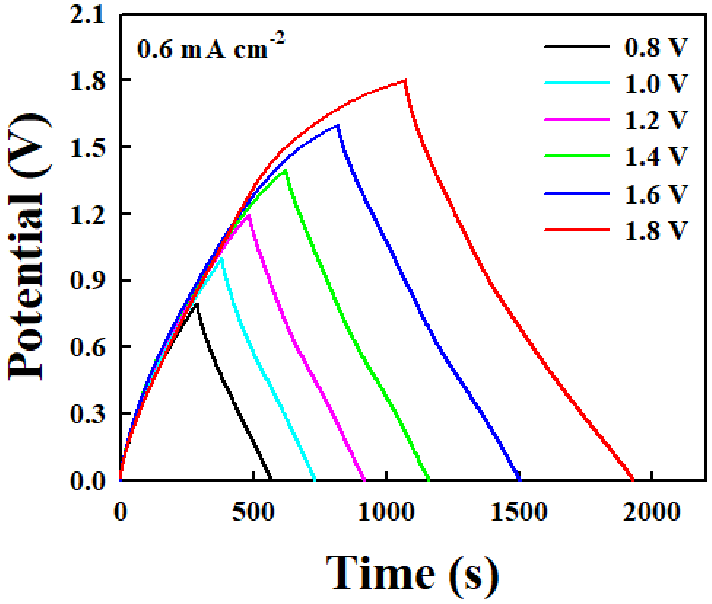

Fig. S18 GCD curves of the Au NP-incorporated 1D-ASCs tested at different voltages from 0.8 to 1.8 V at a current density of 0.6 mA cm^{-2}.

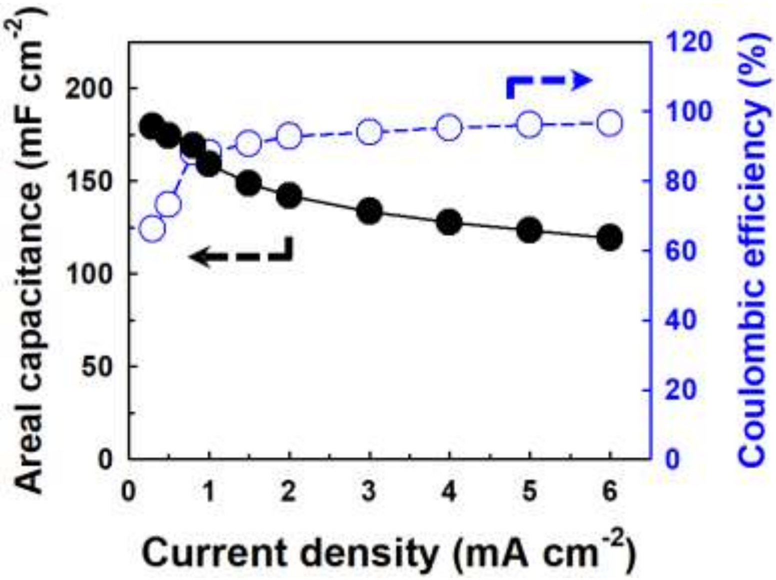

Fig. S19 Areal capacitances and Coulombic efficiency of the Au NP-incorporated 1D-ASCs at different current densities from 0.3 to 6.0 mA cm^{-2}.

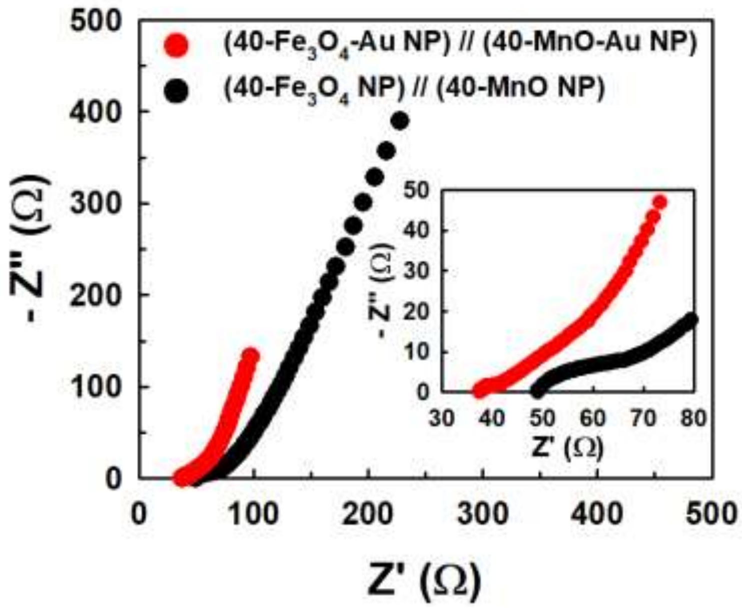

Fig. S20 Nyquist plots of the Au NP-incorporated 1D-ASC and 1D-ASC without Au NPs.

Table S1. Comparison of electrochemical performance of solid-state fiber (or thread) type SCs in two-electrode measurement.

Negative electrode	Positive electrode	Length of electrode (cm)	Electrolyte	Potential (V)	C_A ($mF \cdot cm^{-2}$)	C_V ($F \cdot cm^{-3}$)	C_L ($mF \cdot cm^{-1}$)	C_M ($F \cdot g^{-1}$)	E_A ($\mu Wh \cdot cm^{-2}$) E_V ($mWh \cdot cm^{-3}$) E_L ($\mu Wh \cdot cm^{-1}$) E_M ($mWh \cdot g^{-1}$)	P_A ($\mu W \cdot cm^{-2}$) P_V ($mW \cdot cm^{-3}$) P_L ($\mu W \cdot cm^{-1}$) P_M ($mWh \cdot g^{-1}$)	Ref.
Fe_3O_4-Au NP /MCT	MnO-Au NP /MCT	1.5	Na_2SO_4 /PVA	1.8	179.2 at $0.3 mA \cdot cm^{-2}$	27.9 at $0.3 mA \cdot cm^{-2}$	28.6 at $0.3 mA \cdot cm^{-2}$	7.8 at $0.3 mA \cdot cm^{-2}$	E_A: 80.7 E_V: 12.6 E_L: 12.9 E_M: 3.5	P_A: 3450.1 P_V: 537.7 P_L: 552.1 P_M: 150.5	Our work
		1.5			169.0 at $0.8 mA \cdot cm^{-2}$	26.3 at $0.8 mA \cdot cm^{-2}$	27.0 at $0.8 mA \cdot cm^{-2}$		E_A: 76	P_A: 457.5	
		20			136.7 at $0.8 mA \cdot cm^{-2}$	21.3 at $0.8 mA \cdot cm^{-2}$	21.9 at $0.8 mA \cdot cm^{-2}$		E_A: 61.5	P_A: 457	
CNPs /rGO-CT	CNPs /rGO-CT	1.5	H_3PO_4 /PVA	0.8	-	0.00379 at $50 mV \cdot s^{-1}$	-		E_V: 8.4×10^{-5}	P_V: 0.0564	S12
GHs /MWCNTs-CT	GHs /MWCNTs-CT	1	H_3PO_4 /PVA	0.8	-	-	0.097 at $2 mV \cdot s^{-1}$		E_L: 4.79×10^{-3}	P_L: 1.25	S13
rGO/Ni-CT	rGO/Ni-CT	3.5	LiCl /PVA	0.8	-	68.2 at $50 mV \cdot s^{-1}$	110 at $50 mV \cdot s^{-1}$	311 at $50 mV \cdot s^{-1}$	E_V: 6.1	P_V: 1400	25
PPy/MnO_2 /CNT-CT	PPy/MnO_2 /CNT-CT	-	H_3PO_4 /PVA	0.8	-	-	1490 at $1 mV \cdot s^{-1}$		E_A: 33	P_A: 13000	60
OMC-MnO_2 /CVD gr-CT	OMC-MnO_2 /CVD gr-CT	5	Li_2SO_4/ BMIMCl /PVA	1.5	1100 at $4.3 mA \cdot cm^{-2}$	35.2 at $4.3 mA \cdot cm^{-2}$	-		E_V: 2.7	P_V: 300	S14
rGO/ SWNT@KTP	rGO/ SWNT@KTP	-	H_2SO_4 /PVA	1				366 at $25 mV \cdot s^{-1}$	E_V: 0.29 E_M: 0.0117	P_V: 91000 P_M: 3700	23
rGO /Ni-polyester	rGO /Ni-polyester	-	H_3PO_4 /PVA	0.8	49.4 at $1 mA \cdot cm^{-2}$	-	8.9 at $1 mA \cdot cm^{-2}$		E_A: 1.6	P_A: 2420	36
CF	CF	3	LiCl /PVA	1.2	-	-	32		E_V: 6.8 E_M: 0.052	- P_M: 0.407	26

							at 0.8mA·cm^{-1}				
Activated CF	Activated CF	-	H_3PO_4 /PVA	1.0	-	2.55 at 10mV·s^{-1}	-		E_V: 0.35	P_V: 3000	S15
MWCNT /CMF	CNF film	-	H_3PO_4 /PVA	1.0	86.8 at 2mV·s^{-1}		6.3 at 2mV·s^{-1}		E_A: 9.8 E_L: 0.7	P_A: 8070 P_L: 583	S16
Graphene fiber	Graphene fiber	-	H_2SO_4 /PVA	0.8	390 at 2mV·s^{-1}	78 at 2mV·s^{-1}		350 at 2mV·s^{-1}	E_V: 6.6	P_V: 49	S17
Biscrolled rGO/CNT	Biscrolled MnO/CNT	-	LiCl /PVA	1.2	382.2 at 2.3mA·cm^{-2}	104.7 at 2.3mA·cm^{-2}	17.7 at 2.3mA·cm^{-2}	165.6 at 2.3mA·cm^{-2}	E_A: 35.8		24
CF	MnO_2 /ZnO NWs/CF	-	H_2SO_4 /PVA	1.8	31.15 at10 μA	-	-		E_A: 13.25	P_A: 2120	61
CNT /Carbon paper	MnO_2 /Au wire	-	LiCl /PVA	1.8	12 at 0.3mA·cm^{-2}	-	-		E_A: 5.4	P_A: 2531	62
PPy@CNT film	MnO_2/CF	-	KOH /PVA	1.5	60.43 at 10mV·s^{-1}	9.46 at 10mV·s^{-1}	19.86 at 10mV·s^{-1}	7.72 at 10mV·s^{-1}	E_A: 18.88 E_V: 2.98 E_L: 6.20	-	63
MnO_2 /CNT yarn	MnO_2 /CNT yarn	-	KOH /PVA	0.9	-	25.4 at 10mV·s^{-1}	-		E_V: 3.52	P_V: avg. 127	S18
Fe_2O_3@C /CF	MnO_2/AuPd /CuO /Cu wire	-	LiCl /PVA	1.6	-	2.46 at 130mA·cm^{-3}	-		E_V: 0.85	-	33
GH /Copper wire	MnO_2/RGO /CF	-	KCl /PAKK	1.6	50.8 at 0.2mA·cm^{-2}	2.54 at 0.2mA·cm^{-2}	-		E_A: 18.1 E_V: 0.9	- P_V: 200	34
rGO/Au wire	rGO/Au wire	2	H_3PO_4 /PVA	1.0	0.726 at 2.5μA·cm^{-1}	-	0.0114 at 2.5μA·cm^{-1}		-	-	31
MnO_2/PPy /rGO /Steel fiber	MnO_2/PPy /rGO /Steel fiber	-	H_3PO_4 /PVA	0.8	103 at 11mA·cm^{-3}	12.4 at 11mA·cm^{-3}	-		E_A: 9.2 E_V: 1.1	P_A: 1330 P_V: 160	30
C@Fe_3O_4 /Steel fiber	PEDOT@MnO_2 /Steel fiber	10	LiCl /PVA	2.0	60 at 0.9mA	7.23 at 0.9mA	-		E_A: 33.5 E_V: 4.02 E_L: 5	-	32
$NiCo_2O_4$ /Ni wire	$NiCo_2O_4$ /Ni wire	-	KOH /PVA	1.0	-	1.86 at 0.1mA	-	18.8 at 0.1mA	E_V: 0.21 E_M: 2.18	P_V: 15.5 P_M: 157.5	35

*MCT: metallic cotton thread *CT: cotton thread *CF: carbon fiber *GH: graphene hydrogel *CMC: carboxymethyl cellulose sodium

*CNP: carbon nanoparticle *CMF: carbon microfiber *CNF: carbon nanofiber *AC: activated carbon

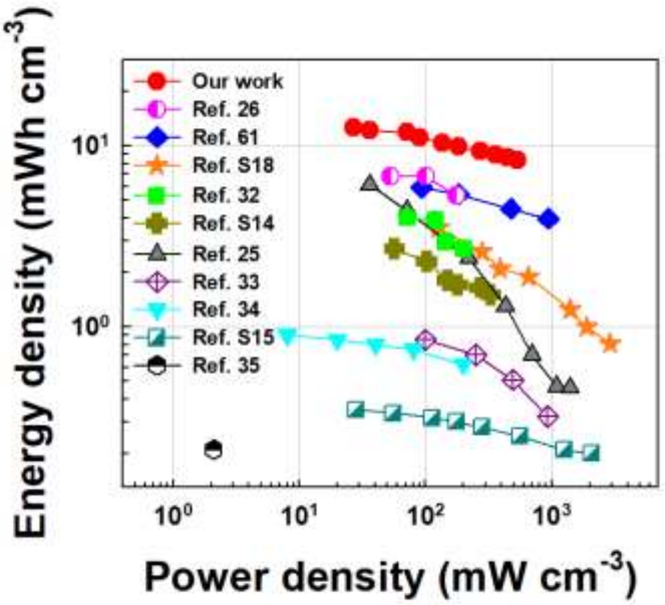

Fig. S21 Ragone plots of the volumetric energy and power density of the Au NP-incorporated 1D-ASCs compared with the solid-state fiber (or thread)-type SCs reported by other research groups.

Notes and references

S1 A. Devia, H.A. Castillo, V.J. Benavides, Y.C. Arango, J.H. Quintero, *Mater. Charact.*, 2008, **59**, 105-107.

S2 T. D. Thanh, J. Balamurugan, S. H. Lee, N. H. Kim, J. H. Lee, *Biosens. Bioelectron.*, 2016, **81**, 259-267.

S3 D. Wilson and M. A. Langell, *Appl. Surf. Sci.*, 2014, **303**, 6-13.

S4 J. Sharma, S. Mahima, B. A. Kakade, R. Pasricha, A. B. Mandale and K. Vijayamohanan, J. Phys. Chem. B, 2004, 108, 13280-13286.

S5 W. Lu, M. Ling, M. Jia, P. Huang, C. Li and B. Yan, *Mol. Med. Rep.*, 2014, **9**, 1080-1084.

S6 M. Guo, J. Balamurugan, X. Li, N. H. Kim and J. H. Lee, *Small*, 2017, **13**, 1701275.

S7 M. M. Vadiyar, X. Liu and Z. Ye, *Chem-SusChem*, 2016, **9**, 932-937.

S8 C.-T. Hsieh, C.-Y. Lin and J.-Y. Lin, *Electrochim. Acta*, 2011, **56**, 8861-8867.

S9 Y. Zhang, P. Chen, X. Gao, B. Wang, H. Liu, H. Wu, H. Liu and S. Dou, *Adv. Funct. Mater.*, 2016, **26**, 7754-7765.

S10 L. Li, X. Zhang, G. Wu, X. Peng, K. Huo and P. K. Chu, *Adv. Mater. Interfaces*, 2015, **2**, 1400446.

S11 V. Khomenko, E. Raymundo-Piñero, F. Béguin, *J. Power Sources*, 2006, **153**, 183-190.

S12 X. Ye, Q. Zhou, C. Jia, Z. Tang, Z. Wan, X. Wu, *Electrochim. Acta*, 2016, **206**, 155-164.

S13 Q. Zhou, C. Jia, X. Ye, Z. Tang, Z. Wan, *J. Power Sources*, 2016, **327**, 365-373.

S14 J. Zhi, O. Reiser, Y. Wang, A. Hu, *Nanoscale*, 2017, **9**, 6406-6416.

S15 D. Yu, S. Zhai, W. Jiang, K. Goh, L. Wei, X. Chen, R. Jiang, Y. Chen, *Adv. Mater.*, 2015, **27**, 4895-4901.

S16 V. T. Le, H. Kim, A. Ghosh, J. Kim, J. Chang, Q. A. Vu, D. T. Pham, J.-H. Lee, S.-W. Kim and Y. H. Lee, *ACS Nano*, 2013, **7**, 5940-5947.

S17 I. Marriam, X. Wang, M. Tebyetekerwa, G. Chen, F. Zabihi, J. Pionteck, S. Peng, S. Ramakrishna, S. Yang and M. Zhu, *J. Mater. Chem. A*, 2018, **6**, 13633-13643.

S18 C. Choi, J. A. Lee, A. Y. Choi, Y. T. Kim, X. Lepró, M. D. Lima, R. H. Baughman, S. J. Kim, *Adv. Mater.*, 2014, **26**, 2059-2065.